Multiphasic bone-ligament-bone integrated scaffold enhances ligamentization and graft-bone integration after anterior cruciate ligament reconstruction

Xianrui Xie [a,c,1], Jiangyu Cai [b,d,1], Dan Li [a], Yujie Chen [a], Chunhua Wang [c], Guige Hou [c], Thorsten Steinberg [e], Bernd Rolauffs [f], Mohamed EL-Newehy [g], Hany EL-Hamshary [g], Jia Jiang [b,****], Xiumei Mo [a,c,*], Jinzhong Zhao [b,**], Jinglei Wu [a,c,***]

[a] State Key Laboratory for Modification of Chemical Fibers and Polymer Materials, Shanghai Engineering Research Center of Nano-Biomaterials and Regenerative Medicine, College of Biological Science and Medical Engineering, Donghua University, Shanghai, 201620, PR China
[b] Department of Sports Medicine, Shanghai Sixth People's Hospital Affiliated to Shanghai Jiao Tong University School of Medicine, Shanghai, 200233, China
[c] School of Pharmacy, Key Laboratory of Prescription Effect and Clinical Evaluation of State Administration of Traditional Chinese Medicine of China, Binzhou Medical University, Yantai, 264003, China
[d] National Engineering Laboratory for Modern Silk, Soochow University, Suzhou, 215123, China
[e] Division of Oral Biotechnology, Center for Dental Medicine, Medical Center – University of Freiburg, Faculty of Medicine, University of Freiburg, Hugstetter Str. 55, 79106, Freiburg, Germany
[f] G.E.R.N. Research Center for Tissue Replacement, Regeneration & Neogenesis, Department of Orthopedics and Trauma Surgery, Faculty of Medicine, Medical Center—Albert-Ludwigs-University of Freiburg, 79085, Freiburg im Breisgau, Germany
[g] Department of Chemistry, College of Science, King Saud University, P.O. Box 2455, Riyadh, 11451, Saudi Arabia

ARTICLE INFO

ABSTRACT

The escalating prevalence of anterior cruciate ligament (ACL) injuries in sports necessitates innovative strategies for ACL reconstruction. In this study, we propose a multiphasic bone-ligament-bone (BLB) integrated scaffold as a potential solution. The BLB scaffold comprised two polylactic acid (PLA)/deferoxamine (DFO)@mesoporous hydroxyapatite (MHA) thermally induced phase separation (TIPS) scaffolds bridged by silk fibroin (SF)/connective tissue growth factor (CTGF)@Poly(L-lactide-co-ε-caprolactone) (PLCL) nanofiber yarn braided scaffold. This combination mimics the native architecture of the ACL tissue. The mechanical properties of the BLB scaffolds were determined to be compatible with the human ACL. *In vitro* experiments demonstrated that CTGF induced the expression of ligament-related genes, while TIPS scaffolds loaded with MHA and DFO enhanced the osteogenic-related gene expression of bone marrow stem cells (BMSCs) and promoted the migration and tubular formation of human umbilical vein endothelial cells (HUVECs). In rabbit models, the BLB scaffold efficiently facilitated ligamentization and graft-bone integration processes by providing bioactive substances. The double delivery of DFO and calcium ions by the BLB scaffold synergistically promoted bone regeneration, while CTGF improved collagen formation and ligament healing. Collectively, the findings indicate that the BLB scaffold exhibits substantial promise for ACL reconstruction. Additional investigation and advancement of this scaffold may yield enhanced results in the management of ACL injuries.

---

1. Introduction

The anterior cruciate ligament (ACL) plays an essential role in connecting the femur and tibia to maintain joint stability in the knee [1]. ACL injuries have become increasingly common due to the global popularity of sports, accounting for 30% of knee injuries [2]. However, the ACL has limited regenerative ability due to factors such as low cell density, inadequate nutrients, and poor blood supply. Currently, ACL reconstruction commonly involves the use of autografts, allografts, or artificial ligaments [3,4]. But, these treatments still face several challenges. For instance, while autografts are considered the gold standard, they can lead to donor site morbidity and compromise the original function of the donor site [5]. The outcome of ACL reconstruction with allografts is often unsatisfactory due to various factors including host immune responses, allergic reactions, disease transmission, and delayed tendon-bone healing [6]. To address these issues, artificial ligaments have gained attention in clinical practice. One example is the Ligament Augmentation Reconstruction System (LARS, France) made of non-degradable polyethylene terephthalate (PET) and has been widely used as an alternative to the native ACL [7]. Although the LARS ligament has shown adequate mechanical properties and improved knee functions, it can also lead to moderate to severe side effects such as synovitis, poor graft-bone healing, and bone tunnel enlargement. These side effects contribute to a high failure rate in long-term follow-up [8]. To achieve ligament regeneration and graft-bone integration, it is crucial to find a bioactive ligament graft with a biomimetic native ACL structure.

Biodegradable natural and synthetic materials have been utilized in the fabrication of scaffolds for ligament tissue regeneration [9,10]. However, these tissue-engineered ligaments lack osteoinductivity and leading to a failure in promoting bone healing upon implantation into the bone tunnel. Consequently, a suboptimal integration between the graft and bone occurs, exacerbating the significant concern of bone tunnel enlargement [11]. To address this challenging problem, it is vital to develop a novel biomaterial composite to enhance ligament-to-bone integration and successfully reconstruct the ACL. In recent years, as biomimicry receives more and more attention, the design of ACL scaffolds should also be a multiphase transition structure to simulate native tissues. For example, Dong et al. introduced a bioactive clay laponite into silk fibroin (SF)/laponite artificial ligament for ACL reconstruction [12]. It promoted the growth of new bone tissue and the generation of fibrocartilage tissue and mature collagen fibers in the bone tunnel segment. Recently, we used biomineralization and electrodeposition methods for depositing calcium phosphate on the PET artificial ligament [3]. The modified scaffolds significantly stimulated the osteogenic differentiation of mouse embryo osteoblast precursor cells (MC3T3-E1) cells and promoted graft-bone integration. However, previous studies have primarily focused on developing ligament-alone grafts. It is believed that incorporating an osteoinductive phase into the ends of a ligament scaffold could generate a multiphasic bone-ligament-bone integrated graft, thus providing better graft-host integration compared with a ligament-alone graft.

A strategy whereby integrating the ligament segment with the bone tunnel segment scaffold resulting in strong bony attachments could circumvent these aforementioned issues and potentially improve the success rate of ACL reconstruction. Electrospun aligned nanofibers or nano/micro hybrid constructions have been proven to promote cell differentiation for ligament tissue engineering applications [13]. However, these densely compacted nanofibers restrict cell infiltration and tissue ingrowth, limiting broader clinical application [14,15]. Besides, electrospun nanofibrous scaffolds possess poor suture-retention strength for surgical reconstruction and generally have insufficient mechanical properties to support primary ligament repair. In contrast, textile scaffolds are widely used in ligament tissue engineering due to their large porosity, sufficient mechanical strength, good flexibility, and retention of the characteristics of constituent units [16–19]. Therefore, by combining electrospun nanofibers with textile scaffolds, it is expected to overcome the aforementioned drawbacks and leverage the respective advantages of both materials. In addition, recent studies have demonstrated that connective tissue growth factor (CTGF), a cysteine-rich matricellular protein, holds significant potential for ligament repair due to its ability to stimulate ligament regeneration by promoting the differentiation of both exogenous and endogenous stem cells. Poly (L-lactide-co-ε-caprolactone) (PLCL) a biodegradable polymer known for its elastic mechanical properties, is commonly employed in various biomedical applications. In this study, we employed PLCL to fabricate core-shell nanofibers with CTGF encapsulated within the fiber component, creating a nanofiber yarn for potential use in ligament repair. Another important aspect of ACL tissue engineering is to choose an appropriate bone scaffold to guide graft-bone integration. Polylactic acid (PLA) is a biodegradable polymer with great mechanical strength and is widely studied and used in the field of bone tissue engineering [20]. In bone tissue engineering, PLA-based scaffolds are commonly utilized as a platform for delivering cells, growth factors, and other bioactive substances (such as hydroxyapatite) to the site of bone defects. We also found the hydroxyapatite (HA) gradient woven scaffold has good osteoinductivity and spatially regulates the differentiation phenotype of bone marrow stem cells (BMSCs) [21]. Furthermore, mesoporous hydroxyapatite (MHA) has the potential to load large numbers of biologically active molecules for drug delivery. The thermally induced phase separation (TIPS) technique has gained significant attention in the fabrication of bone tissue engineering scaffolds due to its simplicity and porosity [22–24]. Although numerous TIPS scaffolds have been extensively studied *in vitro* and *in vivo*, their clinical translation is primarily impeded by insufficient vascularization and weak osteoinductive activity [25]. Deferoxamine (DFO), an iron chelator, has the potential to enhance bone regeneration by promoting angiogenesis through the upregulation of hypoxia-inducible factor-1alpha (HIF-1α) and vascular endothelial growth factor (VEGF) [26].

In this study, a novel bone-ligament-bone (BLB) integrated scaffold was fabricated through the synergistic combination of electrospinning, textile, and TIPS techniques (Fig. 1). A comprehensive investigation was conducted to systematically explore the physicochemical characteristics of the BLB scaffolds. Subsequently, the cytocompatibility, osteogenic potential, and vascularization performance of the scaffolds were assessed through *in vitro* experiments. Furthermore, the ligament and bone regeneration capability of the BLB scaffold was evaluated using the rabbit models.

2. Results

2.1. Characterization of MHA

MHA nanoparticles were synthesized using the hydrothermal method following the procedures in Fig. 1A. The MHA nanoparticles possessed a uniform rod-like shape, measuring approximately100 nm in length and30 nm in width (Fig. 2B). It showed light-colored shaded stripes within the rod-like structure, indicating the presence of nanoporous channels resulting from the removal of cetyl trimethyl ammonium bromide (CTAB) during calcination. The arrangement of these pore channels was primarily disordered, with some degree of order throughout the entire MHA structure. The morphology of DFO@MHA remained unchanged after drug loading, suggesting that the incorporation of small molecular drugs does not significantly impact the structure of MHA (Fig. 2C).

FTIR absorption peaks observed at 1075, 1022, and 940 cm^{-1} corresponded to stretching vibrations of the phosphate group, and 601 cm^{-1} belong to the vibrational mode of OH groups in the HA (Fig. 2D). The strong absorption bands at 2970 and 2960 cm^{-1} were attributed to CH_2 stretching modes of CTAB [27]. Upon calcination, these strong bands disappeared, indicating the absence of residual CTAB species in the calcined sample. The primary crystalline peaks of HA were distributed at diffraction angles of 25.8, 31.8, 32.9, 39.8, and 46.6° (Fig. 2E).
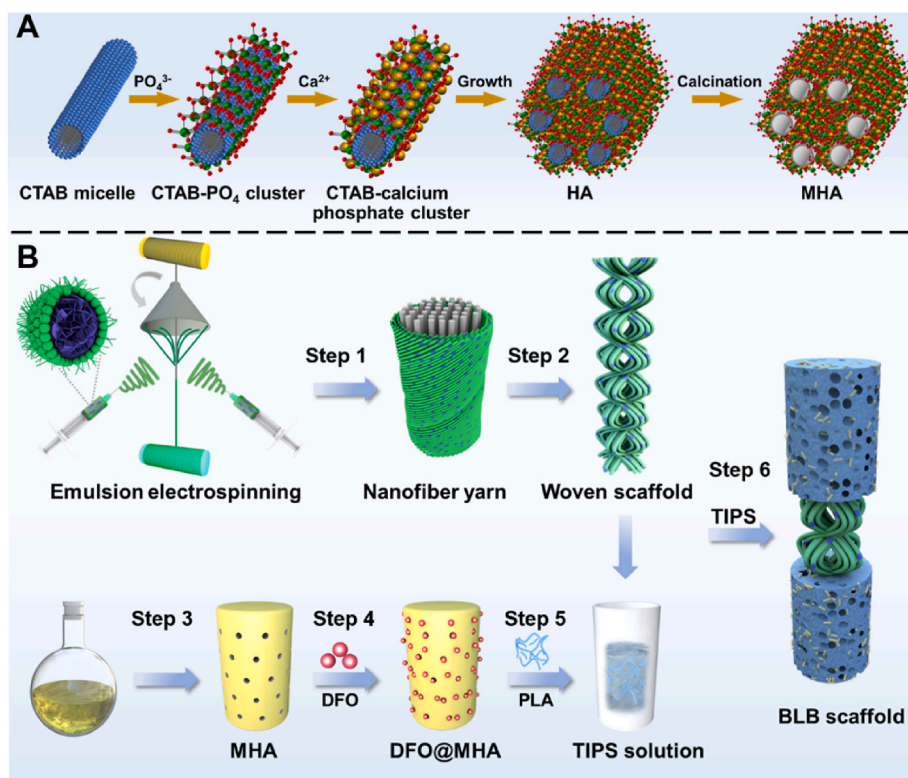
Similarly, the crystalline peaks were observed for MHA at slightly different diffraction angles of 25.9, 31.8, 32.9, 39.9, and 46.8°. XRD analysis showed the MHA possessed a nanocrystalline nature without characteristic diffraction angles of other calcium phosphate phases. The N_2 adsorption-desorption isotherm exhibited a typical type IV pattern (Fig. 2F), further supporting the mesoporous structure of MHA and its successful drug loading ability within the channels [28]. MHA exhibited a specific surface area of 53.1 m^2/g and an average pore size of 4.5 nm (Fig. 2F, insert).

2.2. Fabrication and characterization of BLB integrated scaffolds

The production processes and macroscopic morphology of the BLB scaffolds were schematically illustrated in Figs. 1B and 2G, respectively. Nanofiber yarns loaded with CTGF were prepared by emulsion electrospinning technology (Fig. 2A), and subsequently assembled into a braided scaffold serving as the ligament component of the integrated graft. TIPS technique was used to fabricate bone scaffolds, which were tightly integrated with the braided scaffold (Fig. 2I). MHA and DFO were deposited on PLA to obtain a scaffold loaded with bioactive substances. The BLB scaffold showed a three-section structure, comprising two highly dense TIPS scaffolds at both ends and a soft nanofiber braided scaffold at the center.

The scanning electron microscopy (SEM) images revealed the core-sheath structure of nanofiber yarns with the SF microfibers as the inner core and PLCL or CTGF@PLCL aligned nanofibers as the sheath layer (Fig. 2J). Moreover, the surface of the SF scaffold was smooth while the SF/PLCL and SF/CTGF@PLCL scaffolds became rough and oriented arrangements (Fig. 2K). SEM images exhibited that the PLA, PLA/MHA, and PLA/DFO@MHA scaffolds were porous structures with thin lamellar skeletons (Fig. 2H). The interconnected porous structure with a pore diameter ranging from dozens to hundreds of microns was left in the TIPS scaffolds after freeze-drying. No nanoparticles precipitated on the skeletons of the PLA scaffold. However, the EDS images confirmed MHA or DFO@MHA nanoparticles were uniformly

distributed on the skeletons of PLA/MHA or PLA/DFO@MHA scaffolds through observation of Ca, P, and N elements (Fig. 2H).

The chemical and crystalline structure of the scaffolds were characterized by FTIR (Fig. 3A) and XRD (Fig. 3B), respectively. The PLA characteristic bands in the PLA, PLA/MHA, and PLA/DFO@MHA scaffolds were observed at 1752 (C=O, asymmetric stretching), 1450 and 1382 (C–H, stretching), 1180 and 1082 cm^{-1} (C –O, stretching vibration) [29]. Moreover, MHA nanoparticles presented the characteristic bands located in 559 and 601 cm^{-1} corresponding to the group of PO_4 which appeared for PLA/MHA and PLA/DFO@MHA scaffolds. The SF/PLCL and SF/CTGF@PLCL scaffolds exhibited some similar FTIR spectra, compared to the SF scaffold. The characteristic bands at 1624 and 1514 cm^{-1} corresponded to the amide I region and amide II region of SF, respectively. The characteristic vibration bands were observed at 1756 and 1084 cm^{-1}, attributing to the ester group and C–C stretching of PLCL in the SF/PLCL and SF/CTGF@PLCL scaffolds. In the XRD pattern, PLA shows two characteristic peaks at 16.72° and 19.28°, while the peaks at 31.76° corresponded to the MHA in PLA/MHA and PLA/DFO@MHA scaffolds [30]. SF shows broad diffraction peaks at 9.36°, 20.73°, and 29.43°, indicating that it is a mixed crystal of Silk I (alpha helix) and Silk II (β-sheets). PLCL exhibits a major diffraction peak at 16.80° was confirmed by the semi-crystalline structures. Fig. 3C shows the TGA curves, the thermal decomposition temperature of the PLA, PLA/MHA, and PLA/DFO@MHA scaffolds were in the range of 300–400 °C, and the main chain of PLA molecules was destroyed. The maximum thermogravimetric rates of SF, SF/PLCL, and SF/CTGF@PLCL occur at 300–350 °C, mainly because of the SF degradation. The weight loss above 350 °C was mainly caused by the carbonization and cracking of PLCL polymer. Moreover, the water contact angles of the PLA/MHA (104.1 ± 5.9°) and PLA/DFO@MHA (98.4 ± 5.4°) scaffolds were much lower than the PLA scaffold (130 ± 3.4°) ($p < 0.01$), indicating MHA significantly improved hydrophilic properties (Fig. 3D). The water contact angles of SF, SF/PLCL, and SF/CTGF@PLCL scaffolds were 30.3 ± 2.7°, 40.1 ± 3.4°, and 35.9 ± 4.1°, respectively, and no significant difference ($p > 0.05$).
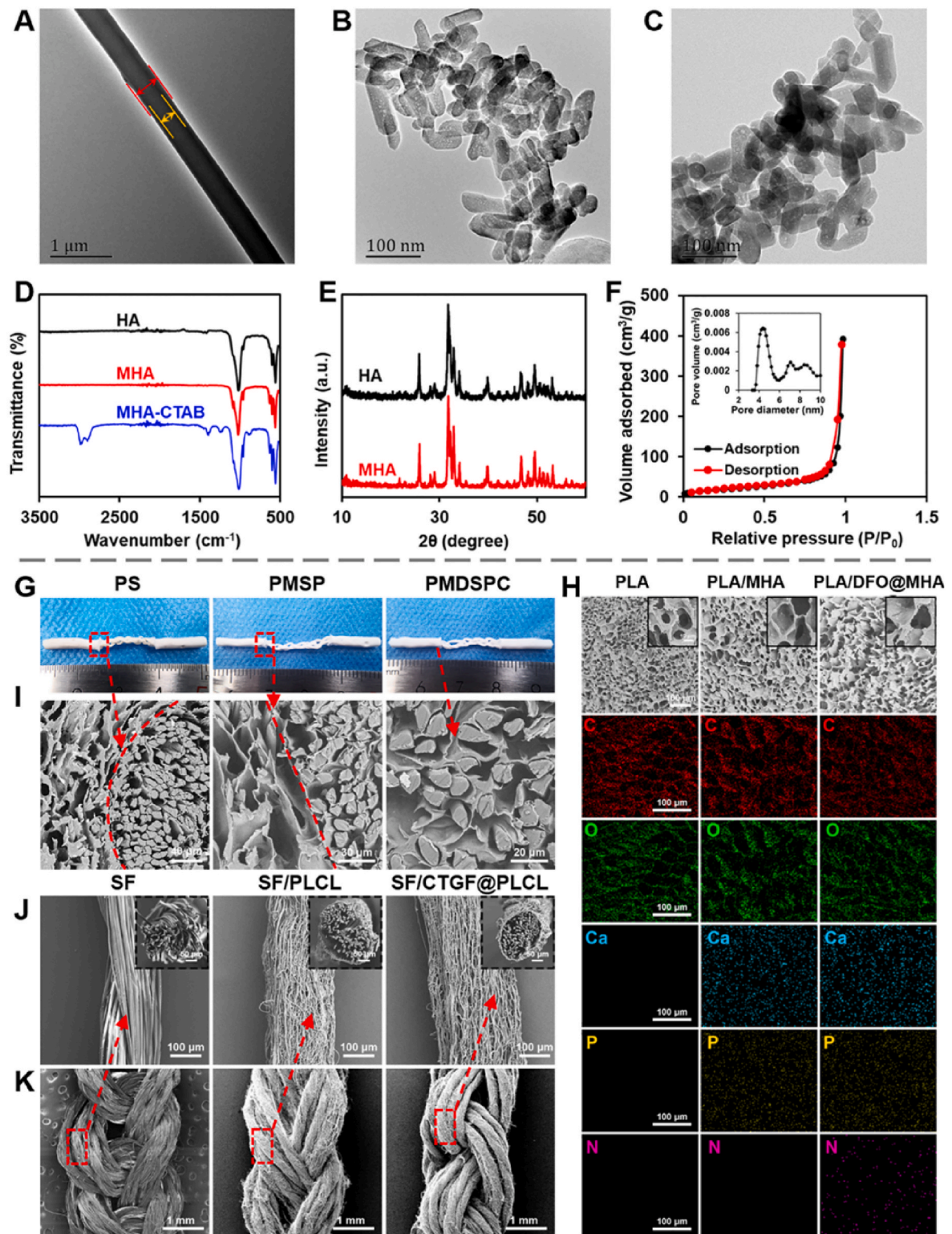
Fig. 2. Microstructure and morphology characterization of nanofibers, MHA, DFO@MHA, and BLB scaffolds. TEM micrographs of (A) nanofibers, (B) MHA, and (C) DFO@MHA. (D) FTIR spectra of HA, MHA, and MHA-CTAB. (E) XRD patterns of HA and MHA. (F) The nitrogen adsorption/desorption isotherms and pore size distribution graph (insert) of the MHA powders. (G) The macroscopic view of three kinds of BLB scaffolds. (I) SEM images of the cross-section of BLB scaffolds. (J and K) SEM images of SF, SF/PLCL, and SF/CTGF@PLCL nanofibers and their braided scaffolds. (H) The SEM images and EDS elemental mappings of PLA, PLA/MHA, and PLA/DFO@MHA samples.
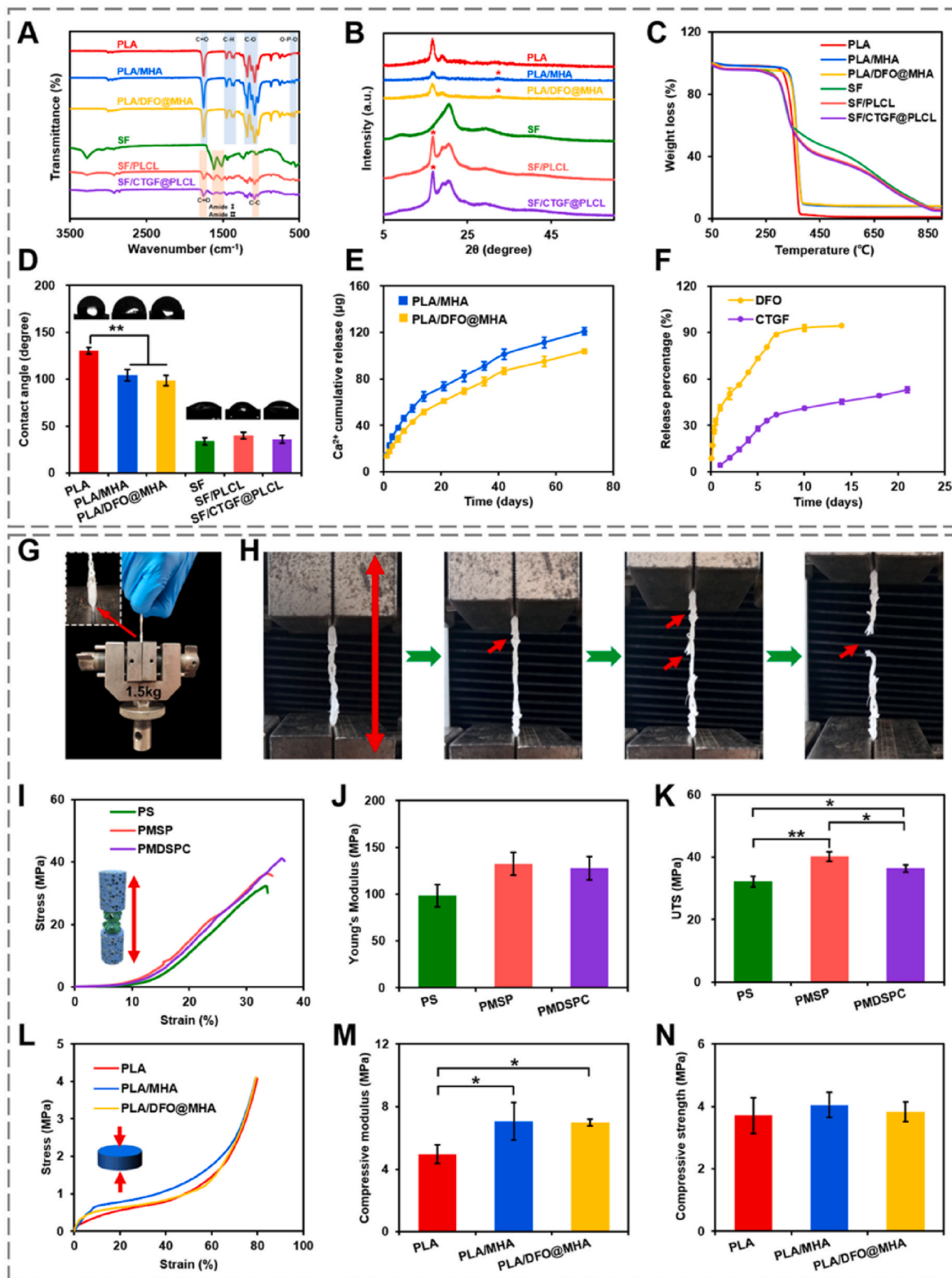
Fig. 3. Characterization and mechanical properties of BLB scaffolds. (A) FTIR spectra, (B) XRD patterns, (C) TGA curves, and (D) water contact angle of PLA, PLA/MHA, PLA/DFO@MHA, SF, SF/PLCL, and SF/CTGF@PLCL scaffolds. (E) The cumulative release amounts of Ca ions were quantified by ICP-AES. (F) *In vitro* the release behaviors of DFO and CTGF from the PLA/DFO@MHA or SF/CTGF@PLCL scaffolds, respectively. (G) Photographs show that the BLB scaffold can support a weight of at least 1.5 kg, about 30,000 times its weight. (H) The BLB scaffolds were placed between the two grips and sustained stretching until it breaks. (I) Representative tensile stress-strain curves, (J) Young modulus, and (K) UTS of BLB scaffolds. (L) Representative compressive strain-stress curves, (M) compressive modulus, and (N) compressive strength of the PLA, PLA/MHA, and PLA/DFO@MHA scaffolds. Statistical analysis was performed by one-way ANOVA followed by Tukey's multiple comparison test, *$p < 0.05$, **$p < 0.01$.

The cumulative release of Ca ions was quantified by ICP-AES and is shown in Fig. 3E. Ca ions were sustainably released from PLA/MHA and PLA/DFO@MHA scaffolds for up to 10 weeks without an obvious burst effect. This release behavior is due primarily to the slow degradation of MHA nanoparticles [21]. The release behavior of DFO or CTGF from the PLA/DFO@MHA or SF/CTGF@PLCL scaffolds is shown in Fig. 3F. DFO had a rapid release profile within 24 h followed by a relatively slow release, with a release period of more than 180 h. The release of CTGF showed an obvious sustained and the accumulated release percentage was $4.3 \pm 1.2\%$ and $53.1 \pm 2.0\%$ on days 1 and 21, respectively.

2.3. Mechanical properties of BLB integrated scaffolds

According to Fig. 3G, the BLB bracket has the ability to withstand 30,000 times its own weight. This remarkable mechanical characteristic indicates that the scaffold fulfills the necessary traction requirements for surgical procedures. On the other hand, when subjected to a specific pulling force, cracks were observed in the TIPS scaffolds. As the tension increased further, the braided scaffold experienced complete fracture, as

illustrated in Fig. 3H. It is worth noting that the TIPS scaffolds consistently maintained tight integration with the braided scaffold, without any detachment during stretching.

The tensile properties of the PLA-SF-PLA (PS), PLA/MHA-SF/PLCL-PLA/MHA (PMSP), and PLA/DFO@MHA-SF/CTGF@PLCL-PLA/DFO@MHA (PMDSPC) scaffolds are summarized in Fig. 3I–K. The Young's modulus of PMSP (132.50 ± 12.29 MPa) and PMDSPC (127.85 ± 12.61 MPa) scaffolds were enhanced significantly as compared with the PS scaffold (98.29 ± 11.85 MPa) ($p < 0.05$) (Fig. 3J). Analogously, the ultimate tensile strength (UTS) in the PMSP (40.23 ± 1.53 MPa) and PMDSPC (36.38 ± 1.15 MPa) scaffolds was significantly higher than that of the PS (32.17 ± 1.67 MPa) scaffold (Fig. 3K), indicating the nanofiber improves the mechanical strength. Importantly, the UTS of the PMSP and PMDSPC scaffolds matched the native ACL (about 35 MPa) of humans [31]. Besides, the strain at failure of the three scaffolds ranged from 31.8% to 35.1% without significant differences ($p > 0.05$) (Fig. S1).

The compression stress-strain curves of PLA, PLA/MHA, and PLA/DFO@MHA scaffolds are shown in Fig. 3L. The PLA/MHA (7.0 ± 1.2
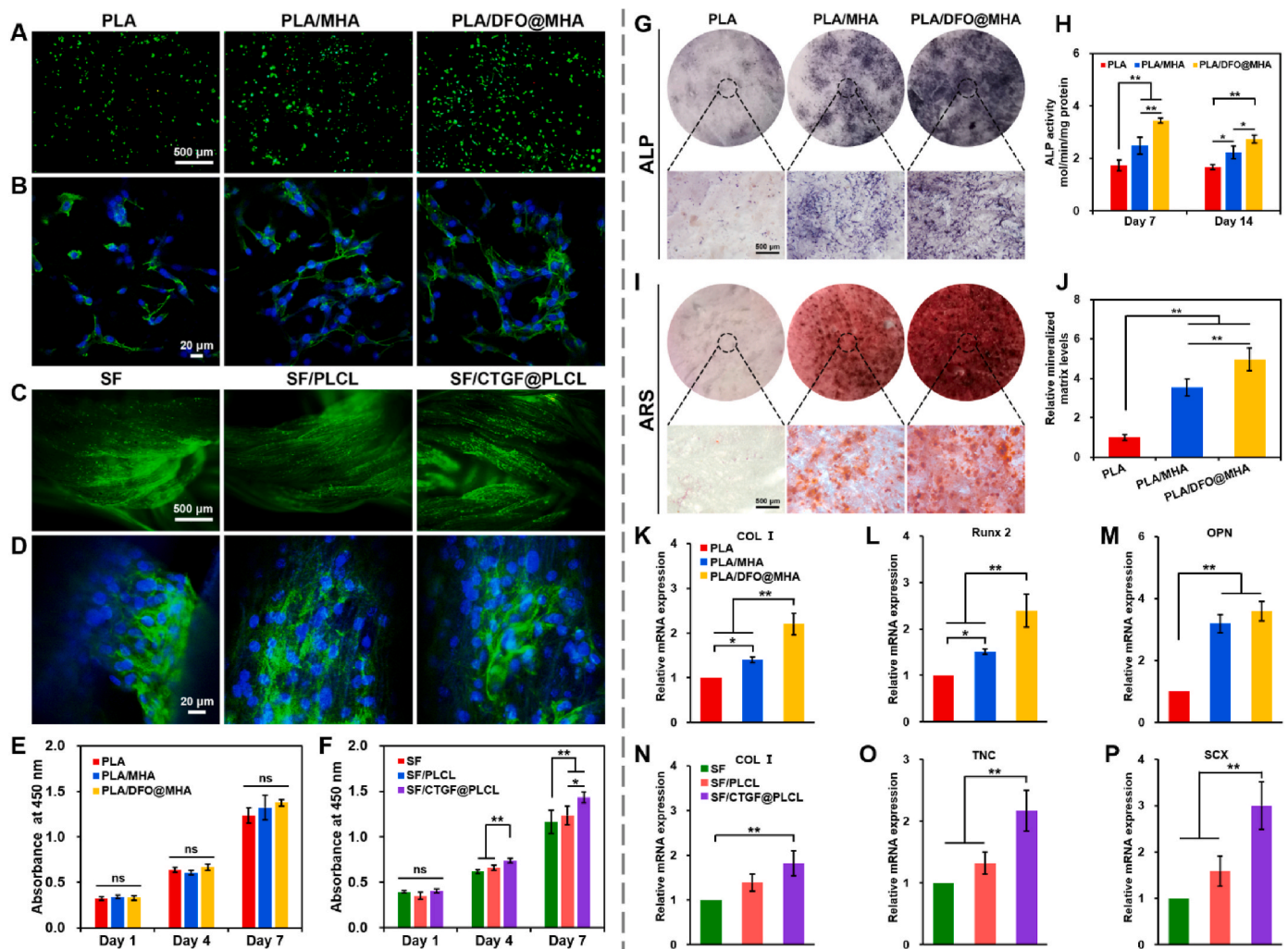

Fig. 4. Cytocompatibility and cell differentiation of BMSCs on scaffolds. (A) Calcein AM (green, live cells) and PI (red, dead cells) staining, (B) Phalloidin (F-actin) and DAPI (nuclei) staining for BMSCs on PLA, PLA/MHA, and PLA/DFO@MHA scaffolds at day 7. (C) Calcein AM (green, live cells) and PI (red, dead cells) staining, (D) Phalloidin (F-actin) and DAPI (nuclei) staining for BMSCs on SF, SF/PLCL, and SF/CTGF@PLCL scaffolds at day 7. (E and F) The cell proliferation of BMSCs cultured on different scaffolds was measured using CCK-8 method. (G) Representative ALP staining images of BMSCs on PLA, PLA/MHA, and PLA/DFO@MHA scaffolds for 7 days, and (H) quantitative analysis of ALP activity for 7 and 14 days. (I) ARS staining and (J) quantitative analysis of BMSCs on PLA, PLA/MHA, and PLA/DFO@MHA scaffolds after osteogenic induction for 14 days. (K–M) The expression of osteogenic differentiation-related genes including COL I, Runx2, and OPN of BMSCs cultured on PLA, PLA/MHA, and PLA/DFO@MHA scaffolds at day 14. (N–P) The expression of ligament differentiation-related genes including COL I, TNC, and SCX of BMSCs cultured on SF, SF/PLCL, and SF/CTGF@PLCL scaffolds at day 14. Statistical analysis was performed by one-way ANOVA followed by Tukey's multiple comparison test, $*p < 0.05$, $**p < 0.01$.

MPa) and PLA/DFO@MHA (7.0 ± 0.2 MPa) scaffolds displayed significantly greater compression modulus than the PLA (4.9 ± 0.6 MPa) scaffold ($p < 0.05$) (Fig. 3M), while the incorporation of MHA afforded no increase in compression strength (Fig. 3N).

2.4. Cell adhesion and proliferation

In vitro assessment of the viability and proliferation of BMSCs on the scaffolds was performed using Live/Dead staining, F-actin staining, and CCK-8 assay. The majority of the cells were living (green) and hardly any dead cells (red) were observed after 7 days of culture on TIPS scaffolds (Fig. 4A). BMSCs on the PLA/MHA and PLA/DFO@MHA scaffolds showed a well-spread and elongated morphology, devoid of distinct individual cell boundaries, indicative of a favorable specific response between the cells and scaffolds (Fig. 4B). However, the distribution of BMSCs on the PLA scaffold was found to be non-uniform, lacking proper spreading. This can be attributed to the hydrophobic nature of PLA, which hinders cell adhesion to the scaffold surface. In contrast, MHA possesses a higher number of bioactive functional groups and exhibits improved hydrophilicity, thus facilitating enhanced interaction between the scaffold and BMSCs. As the culture time increased, the BMSCs gradually proliferated on the PLA, PLA/MHA, and PLA/DFO@MHA scaffolds, and there was no significant difference in absorbance values at the same time point ($p > 0.05$) (Fig. 4E). The results showed that the addition of an appropriate quantity of MHA or DFO to the scaffold did not impede the proliferation of BMSCs.

Live/Dead staining of the SF, SF/PLCL, and SF/CTGF@PLCL scaffolds was predominately living (green) with few dead cells (red) at 7 days (Fig. 4C). Meanwhile, the number of live cells was higher in the SF/CTGF@PLCL scaffold compared to the SF and SF/PLCL scaffolds. Morphological analysis revealed that BMSCs adhered to the SF scaffold in a morphology randomly (Fig. 4D). In contrast, cells adhered to the SF/PLCL and SF/CTGF@PLCL scaffolds displayed an elongated morphology and proliferated along the nanofibers. This observation can be attributed to the aligned arrangement of nanofibers induces the orientation growth and migration of cells [32]. Furthermore, the number of BMSCs on the SF/CTGF@PLCL scaffold was the highest among all groups after culture for 4 and 7 days, indicating that CTGF promotes cell proliferation (Fig. 4F).

2.5. Osteogenic differentiation and related gene expression of BMSCs

Alkaline phosphatase (ALP) activity is an early indicator of osteogenic differentiation and participates in ECM mineral deposition [33]. ALP staining in both PLA/MHA and PLA/DFO@MHA scaffolds exhibited a darker intensity compared to the PLA scaffold at 7 days (Fig. 4G). Quantitative analysis further confirmed that ALP activity in the PLA/DFO@MHA scaffold was significantly higher than that in the other groups (Fig. 4H). Moreover, the PLA/MHA scaffold showed a higher level of ALP activity than the PLA scaffold on days 7 and 14. BMSCs maintained a higher level of ALP activity on the PLA/MHA and PLA/DFO@MHA scaffold, which was attributed to MHA.

Bone mineralization caused by inorganic calcium deposition was deemed a late marker of osteogenic differentiation [3]. The alizarin red staining (ARS) result showed that BMSCs cultured on the PLA scaffold showed minimal calcium nodules, whereas the PLA/MHA and PLA/DFO@MHA scaffolds exhibited extensive areas of osteogenic mineralization (Fig. 4I). Furthermore, the PLA/DFO@MHA scaffold demonstrated a higher formation of distinct mineralized granules compared to the other scaffolds, which were more intuitive under the microscopy. According to the quantitative analysis, the mineralization level of the PLA/MHA and PLA/DFO@MHA scaffolds was greatly enhanced compared to the PLA scaffold (Fig. 4J). Notably, the PLA/DFO@MHA scaffold possesses significantly superior osteoinductivity than the PLA/MHA scaffold on day 14. These findings indicate that MHA promotes the osteogenic differentiation of BMSCs, and the scaffold

incorporating MHA and DFO exhibits greater osteoinductive potential.

To further clarify the effect of scaffolds on the differentiation of BMSCs, the expression of related genes was assessed by RT-qPCR. The results revealed a significant up-regulation of osteogenic-related genes, including Type I collagen (COL I), runt-related transcription factor 2 (Runx2), and osteopontin (OPN) in the PLA/DFO@MHA group compared to the PLA and PLA/MHA groups at 14 days ($p < 0.01$) (Fig. 4K-M). Meanwhile, the PLA/MHA group exhibited higher mRNA expression levels of COL I, Runx2, and OPN than the PLA group at 14 days. These results demonstrated that the MHA and DFO enhance the ability of osteoinductive *in vitro*. Furthermore, BMSCs on the SF/CTGF@PLCL scaffold showed the highest expression levels of ligament-related genes such as COL I, tenascin C (TNC), and scleraxis (SCX) among the three groups (Fig. 4N-P). Encapsulation of CTGF in the SF/CTGF@PLCL scaffold resulted in an increase in the expression of the ligament-related gene.

2.6. Angiogenesis of HUVECs on TIPS scaffolds in vitro

The tube-formation assay was performed to evaluate the effect of DFO on the angiogenesis of human umbilical vein endothelial cells (HUVECs). The tubular network formation of HUVECs in the PLA/DFO@MHA group was significantly increase than the PLA and PLA/MHA groups (Fig. 5A). Although tube formations were observed in both the PLA and PLA/MHA groups, the structures appeared more delicate. The measurement results of the total length of tubules, number of junctions, number of meshes, and total mesh area per high power field showed that all parameters in the PLA/DFO@MHA group were higher than that in the other two groups (Fig. 5B–E). The results indicated that the scaffold loaded with DFO was more comprehensive promotion of vascular tubule formations, thus contributing to the angiogenesis of HUVECs.

The effect of DFO on HIF-1α and VEGF expression was further studied by Western blot. Fig. 5F demonstrates that the expression of HIF-1α and VEGF in the PLA/DFO@MHA group was markedly higher compared to the PLA and PLA/MHA groups after 24 h of culture. The expression level of HIF-1α in the PLA/DFO@MHA group exhibited a 2.1-fold and 1.6-fold increase than the PLA and PLA/MHA groups, respectively (Fig. 5G). Similarly, the HIF-1α downstream targeted gene VEGF, which plays essential roles in angiogenesis, was significantly upregulated in the PLA/DFO@MHA group (Fig. 5H). In summary, the presence of DFO effectively activated the HIF-1α pathway and substantially enhanced VEGF expression in HUVECs, thus promoting the angiogenesis process *in vitro*.

2.7. ACL reconstruction macroscopic observations

The surgical procedure schematic diagram of ACL reconstructed using BLB scaffolds in rabbit models was shown in Fig. 6A and Fig. S2. Gross observations were conducted at 1, 3, and 6 months postoperatively, as shown in Fig. 6B. The repaired ligament exhibited continuous integration with the bone in all rabbits at each time point. The connection between the ligament and the bone was enveloped by fibrous tissue, which demonstrated progressive improvement over time in all three groups. After one month, fibrous-like tissue was observed on the surface of the PMSP and PMDSPC groups, while a thin layer of synovial tissue covered the ligament in the PS group and the scaffold remained distinguishable. After three months, red fibrous connective tissues were apparent in the PS and PMSP groups, indicating an excessive inflammatory response and an inadequate remodeling process. Conversely, the ligament in the PMDSPC group was enveloped by white regenerated tissues. After 6 months, white glossy tissues resembling native ACL ligaments were observed in the PMDSPC group, indicating superior regeneration and remodeling compared to the PS and PMSP groups.
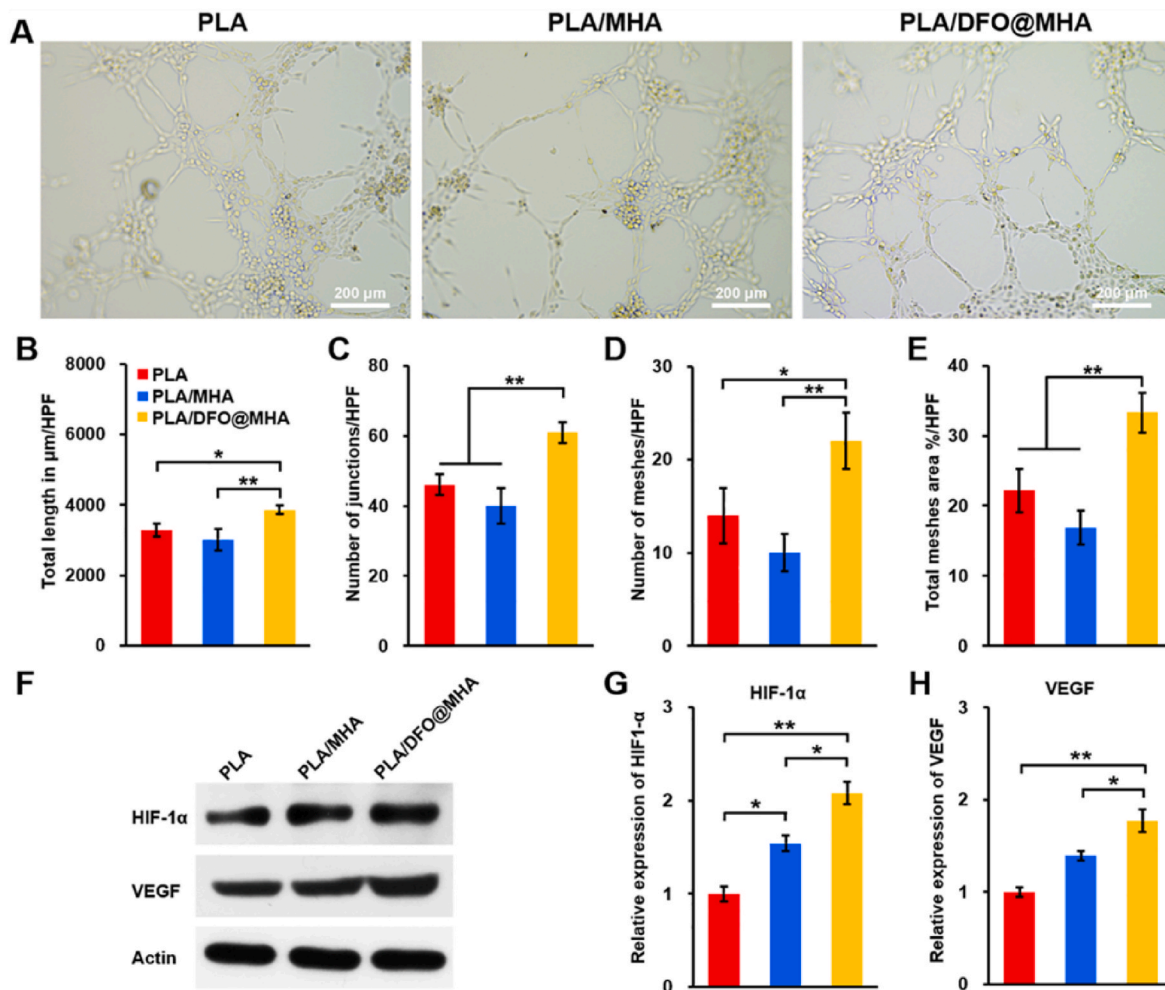
Fig. 5. *In vitro* angiogenesis assay using HUVECs cultured with PLA, PLA/MHA, and PLA/DFO@MHA scaffolds. (A) The images of tubule networks formation in HUVEC after culturing with various samples on Matrigel for 6 h. Summarized data showing the difference of (B) total length, (C) the number of junctions, (D) the number of meshes, (E) total meshes area per high power field (HPF) in HUVECs. (F) Representative western-blot images showing the expression of HIF-1α and VEGF in HUVECs cultured with various groups for 24 h. Summarized data showing the difference in (G) HIF-1α and (H) VEGF expression based on the western-blot results. Statistical analysis was performed by one-way ANOVA followed by Tukey's multiple comparison test, $*p < 0.05$, $**p < 0.01$.

2.8. Histological analysis of the regenerated ligament

Picrosirius Red staining was used to evaluate the regeneration and remodeling of collagen fibers [34]. As shown in Fig. 6C, the regenerated collagen fibers exhibited an increasing level of maturation over time and exhibit a crimp morphology, as evidenced by the birefringence of collagen. At three and six months post-surgery, the brightness of the PMDSPC group was significantly higher than that of the PS and PMSP groups, indicating the formation of a more mature and remodeled collagen matrix in the PMDSPC group, especially collagen type I. Moreover, hematoxylin and eosin (HE) staining showed inflammatory cell infiltration and foreign-body responses in all three groups at 1 month (Fig. 6D). After three months, the scaffolds experienced partial degradation, and regenerative tissues gradually formed around them. Notably, a greater amount of new tissue was observed around the scaffold in both the PMSP and PMDSPC groups compared to the PS group, with some tissue even growing into the interspaces of the scaffold. Both PMSP and PMDSPC groups displayed regenerated aligned fibrous tissue at 6 months, with the PMDSPC group demonstrating a higher degree of maturation and alignment. Remarkably, the PMDSPC group exhibited a structure reminiscent of native ligaments, characterized by well-organized bundles of highly crimped collagen fibers.

Furthermore, immunofluorescence staining was employed to assess the remodeling of collagen. Over time, there was gradual improvement in the deposition of COL I (red bright area) among the three groups (Fig. 6E and Fig. S3A). The PMDSPC group showed a more organized collagen structure and a greater abundance of COL I matrix than the other groups. The regenerated COL I fibers in the PMDSPC group exhibited a crimp morphology, while the COL I in the PS group displayed a disordered arrangement with limited maturity. The expression of COL III was lower in the PS and PMSP groups upon CTGF delivery from the PMDSPC scaffold, indicating potential enhancement in the healing of ligamentization process (Fig. 6F and Fig. S3B). On balance, the results indicate that the ligament healing process has reached a stage characterized by substantial collagen ECM formation and is continuing toward the remodeling process.

2.9. Biomechanical tests

As shown in Fig. 6G and H, the failure load of the PMDSPC group (59.3 ± 7.8 N) was significantly higher than that of the PS group (43.5 ± 3.4 N) and PMSP group (47.2 ± 4.8 N) at 3 months after surgery. At 6 months, the failure load of the PMDSPC (89.0 ± 3.2 N) group and PMSP groups (67.3 ± 4.6 N) was significantly higher than that of the PS group (55.1 ± 3.8 N). The PMDSPC group had the highest failure load among the three groups. Meanwhile, the stiffness of the PMDSPC group (21.7 ±
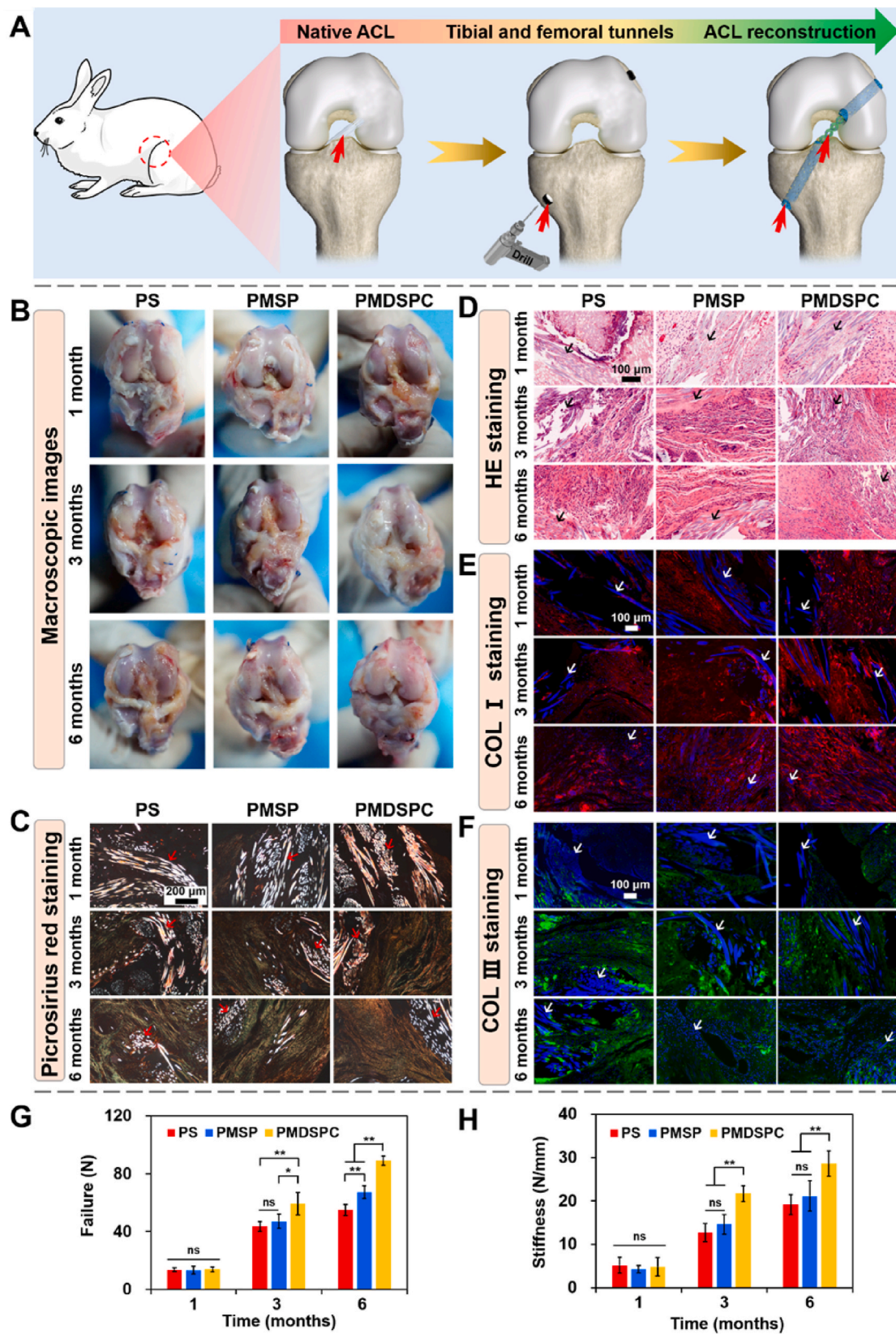
Fig. 6. Histopathological and biomechanical analysis of the new formed tissue within the implanted BLB scaffolds. (A) Schematic diagram of BLB scaffolds used for ACL reconstruction surgery in rabbit models. (B) The macroscopic view of regenerated ACL in different groups at 1, 3, and 6 months postoperatively. (C) Picrosirius red, (D) HE, (E) COL I, and (F) COL III staining of the regenerated ligament in three groups at 1, 3, and 6 months postoperatively, the arrow indicates the implanted grafts. (G and H) The biomechanical analysis of regenerated ACL in each group at 1, 3, and 6 months postoperatively. The detection items are (G) ultimate failure load and (H) stiffness. Statistical analysis was performed by one-way ANOVA followed by Tukey's multiple comparison test, $*p < 0.05$, $**p < 0.01$.

1.8 N/mm for 3 months; 28.6 ± 2.9 N/mm for 6 months) was significantly higher than that of PS (12.7 ± 2.1 N/mm for 3 months; 19.2 ± 2.3 N/mm for 6 months) and PMSP (14.6 ± 2.3 N/mm for 3 months; 21.2 ± 3.5 N/mm for 6 months) groups at 3 and 6 months after surgery, respectively.

2.10. Histopathological and Micro-CT analysis of bone tunnels

The process of graft-bone integration guided by the BLB scaffold was performed using histological staining. HE staining revealed no severe inflammatory response or tissue necrosis in any of the groups (Fig. 7A). After one month, there was a clear interface gap between the bone tissue and the graft in all three groups. Over time, the interface width gradually decreased in each group, indicating the growth of new tissue into the scaffold. After 3 and 6 months, new bone formation was observed at the defect margins in the PS and PMSP groups. In contrast, a significant amount of newly formed bone was present at the margin of the defect and filled inside the PMDSPC scaffold. The Masson staining images are shown in Fig. 7B, the PMDSPC group had more new bone formation compared to the other groups, which was consistent with the HE staining results. In addition, dense collagen fibers appeared in the area around the PMDSPC scaffold, while only a small amount of loose collagen deposition in the PS and PMSP groups at 1 month. Importantly, the PMDSPC group showed a larger area of mature bones compared to the other groups. These findings suggest that the loading of MHA and DFO into the scaffolds may have a synergistic effect in promoting the maturation of regenerated bone, thereby facilitating the repair of bone tunnel defects. The effect of DFO released by the PMDSPC scaffold on angiogenesis was evaluated using immunofluorescence staining of α-smooth muscle actin (α-SMA) and HIF-1α (Fig. 7C). The quantitative analysis indicated that the expression of α-SMA (15.1%) and HIF-1α (18.2%) in the PMDSPC group was significantly higher than that in the PS and PMSP groups (Fig. 7D–E, $p < 0.01$). This indicated that the local release of DFO activates the HIF-1α pathway, resulting in the upregulation of α-SMA protein expression during the bone repair process.

The effects of different scaffolds on new bone tissue formation were observed in the femoral bone tunnels using two-dimensional and three-dimensional reconstructed micro-CT images (Fig. 7F and G). At an early stage (1 month), minimal new bone formation was observed within the bone tunnel (as circled in red) among all groups. Subsequently, new bone tissue gradually extended from the tunnel edge towards the interior. The new bone integration of the PMSP group was better than that of the PS group, but inferior to the PMDSPC group at 3 and 6 months. After 6 months, the PMDSPC group showed the largest area of newly formed bone with a higher density, suggesting superior bone repair efficiency. Quantitative measurements of the bone tunnel are presented in Fig. 7H and I. At one month, there were no significant differences in the bone tunnel area and bone volume to total volume ratio (BV/TV) value among the three groups ($p > 0.05$). At 3 and 6 months, the average bone tunnel areas in the PMSP and PMDSPC groups were much lower than those of the PS group, with the PMDSPC group exhibiting the smallest area ($p < 0.01$). Besides, the BV/TV value of the PS group decreased continuously from the first (10.8 ± 1.2%) to the sixth month (5.6 ± 0.6%). Conversely, the BV/TV value in both the PMSP (10.9–15.4%) and PMDSPC (11.0–18.9%) groups gradually increased over time. These results demonstrate that the combination of MHA and DFO prominently enhances the osseointegration of the BLB scaffold.

3. Discussion

The ideal ligament tissue engineering scaffold should be able to restore the normal anchoring structure of the native ACL as much as possible to ensure joint function after reconstruction [11]. However, to date, no ligament scaffold can fully meet the requirements of ACL reconstruction, and the poor integration between the scaffold and bone continues to face challenges. Thus, this study aimed to research the potential of novel multiphasic BLB integrated scaffolds to enhance tendon-bone healing and achieve ACL reconstruction. The results demonstrate that the BLB scaffold loaded with CTGF and DFO achieves most favorable effect after ACL reconstruction among all the groups.

Composite scaffolds are anticipated to serve as a promising clinical intervention for modulating the adverse microenvironment of bone defects and surmounting the hurdles encountered in bone regeneration. The amalgamation of synthetic organic polymers and inorganic minerals exploits the advantages of both materials, a crucial consideration given the intricate nature of the targeted repair sites. Numerous studies have demonstrated the efficacy of PLA scaffolds in promoting bone healing and regeneration both *in vitro* and *in vivo* [29,35]. However, challenges remain, such as its hydrophobicity hampers cell adhesion, and the acid degradation product lactic acid has been found to induce a mild aseptic inflammatory response *in vivo* [36]. HA, a native mineral compound is a well-established material for bone regeneration. Previous research has extensively employed HA as a filling material to prepare biocompatible matrices in orthopedic and mineralized implants [37]. Consequently, the incorporation of MHA into PLA scaffolds appears to be a reasonable approach [38]. Furthermore, several studies have demonstrated the promising results of DFO in promoting bone repair in animal fracture models. Steven et al. successfully showed the beneficial effects of locally delivering a low dose of DFO using bioresorbable bone substitutes [39]. Therefore, DFO serving as the active ingredient was chosen to enhance the vascularization and osteogenic properties of the scaffold. In a separate study, Drager, J. et al. injected DFO solution directly every 48 h after graft implantation, but repeated injections were necessary due to the short half-life of DFO being only 5.6 h [40]. The rapid drug metabolism hindered the application of DFO in the treatment of large-segment bone defects. To solve the above problems, the DFO@MHA system with stable physical and chemical properties, as well as controllable drug release properties were constructed. In this drug delivery system, the complete release of DFO was over 160 h, and the sustained release process prolongs the duration of action for a better therapeutic effect.

HA has been extensively studied for its outstanding biocompatibility and osteoinductivity, which are crucial for promoting bone growth during tendon-bone healing [41]. Several studies have reported that HA plays a pivotal role in the regulation of cell adhesion, migration, proliferation, and differentiation, thereby contributing significantly to bone development, growth, and remodeling [42]. Jiang et al. evaluated the ability of the injectable HA/COL I paste to promote tendon-bone healing and their findings that the HA component in the paste could regulate the osteogenic expression and enhance the tendon-bone interface healing [41]. In our previous studies, we observed that scaffolds incorporated with HA not only promoted the proliferation of MC3T3-E1 cells but also stimulated the osteogenic differentiation of BMSCs [21]. In this work, we investigated the effect of a sustained release of a low dose of calcium ions on the osteogenic differentiation of BMSCs, which is crucial for the formation of a bony layer in osseointegration. *In vitro* study, the release of calcium ions from the PLA/MHA and PLA/DFO@MHA scaffolds significantly increased the ALP and ARS activity of BMSCs, indicating enhanced osteogenic differentiation (Fig. 4G–J). Furthermore, the expression of osteogenic differentiation markers, such as COL I, Runx2, and OPN, was upregulated by the incorporation of MHA (Fig. 4K-M). Overall, the incorporation of MHA into the PLA scaffold improved the biological activity of the grafts and promoted the production of the corresponding extracellular matrix.

Vascularization is a critical factor for the achievement of bone regeneration owing to the strong correlation between osteogenesis and angiogenesis [43]. Osteogenesis and angiogenesis mutually support each other during bone remodeling. Neovascularization supplies nutrients for bone remodeling, and certain osteogenic proteins also promote angiogenesis [44]. HIF-1α serves as the primary transcriptional regulator in hypoxia induction and plays important roles in the coupling of angiogenesis and osteogenesis during bone remodeling and bone
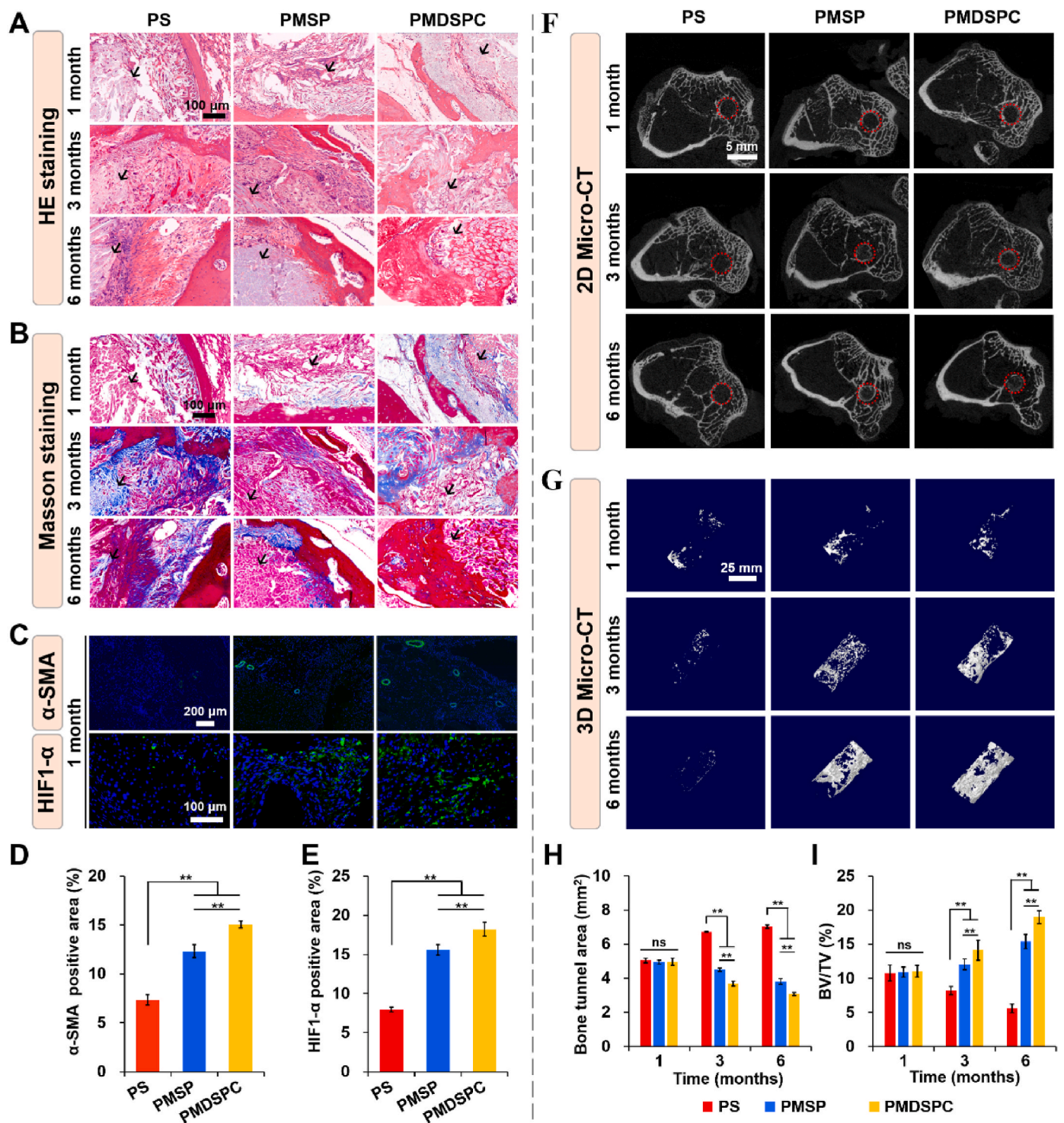
Fig. 7. Histopathological and Micro-CT imaging analysis of bone tunnels in different groups after surgery. Representative images of (A) HE, and (B) Masson staining of the decalcificated bones slice after implantation of various scaffolds for 1, 3, and 6 months. Black arrows indicate the implanted grafts. (C) Representative immunofluorescence histochemical images of HIF-1α and α-SMA staining of the decalcificated bones slice after implantation of various scaffolds for 1 month. (D and E) Quantitative analysis of the positively stained areas using Image-Pro Plus software based on the immunofluorescence histochemical images of HIF-1α and α-SMA. (F) Micro-CT images of the cross-sections of the femoral bone tunnels and (G) three-dimensional reconstructed micro-CT images showing the effect of different scaffolds on the new bone tissue formation inside the defect site. The bone defect area was circled by a dotted line (red). (H and I) The average bone tunnel area, and BV/TV values were calculated using the CT-Analyzer software after 1, 3, and 6 months. Statistical analysis was performed by one-way ANOVA followed by Tukey's multiple comparison test, $*p < 0.05$, $**p < 0.01$.

regeneration, thereby offering a novel concept for the development of bone repair biomaterials that are prone to early-stage vascularization in the bone repair process [45]. As a potent activator of HIF-1α, the release of DFO from the scaffold promotes angiogenesis by generating angiogenic factors and stimulating the migration of HUVECs. Previous studies have demonstrated that DFO induces the upregulation of HIF-1α and its downstream effector VEGF in cells [46]. In our *in vitro* investigation, we observed that DFO treatment led to a significant increase in the protein expression levels of both HIF-1α and VEGF in HUVECs (Fig. 5). Subsequently, *in vivo* study, the PMDSPC scaffold exhibited the potential to promote angiogenesis, as evidenced by the immunofluorescence staining for HIF-1α and α-SMA in the regenerated bone tissue at the one-month postoperative stage (Fig. 7C–E). Furthermore, neovascularization was also present in the PMSP group, which can be attributed to the release of calcium ions by the MHA during hydration and hydrolysis, then recruits VEGF to improve angiogenesis and bone calcification [47]. For the PMDSPC group, DFO and calcium ions were released simultaneously and sustainably from the scaffold, resulting in a sustained synergistic effect during the bone regeneration process (Fig. 7F–I). The synergistic action of the dual delivery system, involving DFO and calcium ions from the PMDSPC scaffold, elucidates the underlying mechanism responsible for the enhanced bone regeneration observed in our study.

CTGF has been demonstrated to enhance the regeneration of ligament by inducing differentiation of both exogenous and endogenous stem cells into ligament fibroblasts [48]. In this study, we used emulsion electrospinning to load CTGF onto nanofiber yarns, creating a sustained delivery system. We further investigated the impact of CTGF on the differentiation of BMSCs and its role in ligament healing. Through the upregulation of COL I, TNC, and SCX, which are markers associated with ligament formation, CTGF successfully induced the differentiation of BMSCs into ligament fibroblasts. However, the specific molecular mechanisms underlying this process remain poorly understood. Li et al. discovered that CTGF induces tenogenic differentiation of adipose-derived stem cells *via* the FAK and ERK1/2 signaling pathways [48]. Additionally, Cong et al. reported that the AKT-mTOR signaling pathway is activated during tenogenesis in BMSCs [49]. These findings provide new insights into the cellular and molecular mechanisms involved in ligament differentiation. Our *in vivo* data demonstrated that CTGF regulates COL I expression and native-like collagen fibers orientation and composition for ACL repair in rabbits (Fig. 6B–F). The delivery of CTGF along the PMDSPC scaffold track may accelerate and guide the ligament repair processes. Interestingly, a new role of CTGF was suggested in modulating macrophage polarization, which likely plays important role in ligament healing. Previous research has shown that CTGF attenuates tendon inflammation, resulting in decreased IL-1β and IL-6 expression and inflammatory cell infiltration during flexor tendon healing [50]. Consistent with previous findings, our *in vitro* and *in vivo* results provide support for the notion that CTGF has the potential to decrease ligament inflammation (Fig. S4) and promote ligament healing.

While the BLB scaffold holds great promise for ACL reconstruction, our current study has identified several limitations. The exact mechanism through which CTGF induces proliferation and differentiation of BMSCs remains poorly understood. Further studies will aim to gain a more comprehensive understanding of the key signaling pathways involved in CTGF regulation of stem cell function. In addition, it is worth noting that our animal experiment utilized New Zealand white rabbits as subjects, which are small animals, and the observation period was relatively short. The mechanical characteristics and lower extremity alignment of quadrupedal animals differ from those of the bipedal human knee. Despite the excellent outcomes in the rabbit model, experiments using large animal models should be performed to extrapolate the results to humans. Therefore, the utilization of a large animal model (such as beagle or pig) and long-term observations are imperative to validate the properties of the BLB.

4. Conclusions

In summary, the multiphasic BLB integrated scaffolds were developed using a combination of electrospinning, textile, and TIPS processing techniques. The BLB scaffolds exhibited a three-phase structures and excellent mechanical properties, resembling the biomimetic nature of native ACL tissues. *In vitro* study revealed that the incorporation of CTGF into the nanofibrous braided scaffolds significantly enhanced the expression of ligament-related genes in BMSCs, and promoted cell proliferation and migration. Furthermore, the PMDSPC scaffold facilitated osteogenic differentiation of BMSCs and promoted the migration and tubular formation of HUVECs, with the involvement of the HIF-1α signaling pathway. Moreover, in a rabbit model of ACL reconstruction, the BLB scaffolds demonstrated remarkable efficacy in promoting ligament and bone tissue regeneration, enhancing graft-bone integration, and accelerating the ligamentization and graft-bone integration processes. Particularly, the PMDSPC scaffold induced the formation of ligament tissue and facilitated extensive new bone tissue ingrowth into the interface, resulting in the superior biomechanical properties observed at 6 months compared to the other two groups. Therefore, the BLB scaffold exhibits great potential for application and may serve as an alternative to conventional techniques for ACL reconstruction in the future.

5. Experimental section

Materials: Calcium chloride (CaCl$_2$, ≥96%), disodium hydrogen phosphate (Na$_2$HPO$_4$, ≥99%), sodium hydroxide (NaOH, ≥96%), and dioxane (C$_4$H$_8$O$_2$) were purchased from Sinopharm Chemical Reagent Co., Ltd. PLCL, a copolymer of PLCL with ʟ-lactide to the ε-caprolactone ratio of 75 to 25, from Gunze Medical Devices Limited, Japan. L- PLA was obtained from Jinan Daigang Biomaterial Co., Ltd (Shandong, China). 1,1,1,3,3,3-Hexafluoro-2-propanol (HFIP) was purchased from Shanghai Darui Finechemical CO. Ltd. CTAB and span-80 was purchased from Aladdin Biochemical Technology Co., Ltd (Shanghai, China). DFO and Matrigel medium were purchased from Sigma-Aldrich (Shanghai, China). CTGF was purchased from PeproTech (USA). The regenerated SF was prepared as previously reported.

Synthesis and Drug Loading of MHA: MHA powders were synthesized by a hydrothermal method as previously reported [51]. The detailed methods are provided in Supplementary Information.

Fabrication of nanofiber yarns and braided scaffold: The electrospinning emulsion solution was configured as the method previously reported by our group [52]. The nanofiber yarn with a core-shell structure was prepared by a commercial electrospinning apparatus (Fig. 1B), and refer to our previous reports for specific preparation methods [21]. The detailed methods are provided in Supplementary Information. Subsequently, the SF, SF/PLCL, and SF/CTGF@PLCL yarns were weaved manually to produce SF, SF/PLCL, and SF/CTGF@PLCL fabrics as ligament scaffolds. Briefly, ten yarns were combined into a single strand and then intertwined into a scaffold similar to a "braids" structure.

Fabrication of BLB integrated scaffold: PLA was dissolved in dioxane at 60 °C to make a PLA solution of 8% (wt/v), then MHA or DFO@MHA (10% of PLA mass) was added to the PLA solution, and sonicated for 15 min to obtain a homogeneous solution of PLA/MHA or PLA/DFO@MHA. The BLB integrated scaffolds were fabricated by TIPS. Briefly, both ends of the SF braided scaffold were placed inside cylindrical molds, and then the PLA solution was cast into the mold. The whole system was kept at −20 °C for 1 h and then maintained at −80 °C for 48 h. When the PLA was completely frozen, the whole system was lyophilized to obtain the PS scaffolds. The PMSP and PMDSPC scaffolds were fabricated by the same method. Besides, separate SF, SF/PLCL, SF/CTGF@PLCL, PLA, PLA/MHA, and PLA/DFO@MHA scaffolds were fabricated for subsequent experimental study.

Characterization: Characterization of MHA and BLB integrated scaffold including surface and inner morphological, chemical structure,

thermal gravimetric analysis, surface hydrophilicity, nitrogen adsorption/desorption isotherms, and tensile test were performed. The release behavior of Ca^{2+}, DFO, and CTGF were determined and more details in the Supporting Information.

Cell viability and tube formation assay of HUVECs: BMSCs were obtained from the bone marrow of SD rats according to the previous study [53]. The detailed methods are given in Supplementary Information.

In vitro mineralization: The ALP and ARS activities were performed and more details in the Supporting Information.

Gene and Protein expression analysis: The primer sequences are listed in Table S1. More details in the Supporting Information.

ACL reconstruction animal model: Animal experiments procedures were approved by the Animal Research Committee of Shanghai Jiao Tong University Animal Science Department (NO.2018-0006). Sixty-three New Zealand white male rabbits (weight from 3.0 to 3.5 kg) were randomized into the three groups with 21 rabbits in each group for 3-time points. BLB scaffolds that fit the size of the ACL of the rabbit knee joint were customized. Under aseptic conditions, the ACL reconstruction procedure was performed according to our previous study [54]. Briefly, anesthesia was induced by intramuscular injection of 0.8 mL of xylazine hydrochloride and 0.8 mL of diazepam. The native ACL was exposed *via* a medial parapatellar approach and was excised. Tibial and femoral tunnels with a diameter of 2.5 mm were drilled along with the original ACL footprint. Subsequently, the BLB scaffold was pulled into the tibial tunnel and passed through the femoral tunnel using a PDS-II suture (Ethicon, Puerto Rico, USA). Both ends of the scaffold were sutured with the adjacent periosteum and soft tissue, and the wound was closed layer by layer. The animals were returned to the cages for free activities and followed by an injection of penicillin with 100,000 U/kg for 3 days after surgery. The rabbits were sacrificed at 1, 3, and 6 months postoperatively, and the regenerative tissue samples were harvested for further evaluation.

Histological and immunofluorescence assessment: The regenerative tissues were examined by HE staining, Masson staining, and immunofluorescence staining analysis. More details in the Supporting Information.

Micro-CT analysis: At 1, 3, and 6 months after surgery, the femur specimens were scanned at a spatial resolution of 35 μm (1 mm aluminum filter, 65 KV, 380 μA) using a Skyscan 1176 micro-CT imaging system (Bruker, Kontich, Belgium) to analyze the graft osseointegration process in the bone tunnel. After that, the BV/TV value was calculated using the CT-Analyzer software (DataViewer, CTvol, and CTAn).

Biomechanical test: After sacrifice, the femur-graft-tibia complex was harvested from each knee joint and immobilized firmly in clamps of the mechanical testing instrument (Instron 5966, USA). A preload of 1 N followed by a load displacement rate of 5 mm min^{-1} was applied to the specimen until rupture or the graft was pulled out from the bone tunnel. The failure load was recorded from the load-displacement curve, and the stiffness was calculated from the slope of the linear region of the curve.

Statistical analysis: Data were expressed as mean ± standard deviation (SD). Statistical analyses were performed using Origin 9.1 software. One-way analysis of variance (ANOVA) followed by Tukey's post hoc test was used to determine the statistical significance unless specified otherwise. The significant difference was considered at *$p < 0.05$ and **$p < 0.01$.

CRediT authorship contribution statement

Xianrui Xie: Conceptualization, Methodology, Writing – original draft, Validation, Data curation, Visualization. **Jiangyu Cai:** Conceptualization, Methodology, Writing – review & editingWriting – Editing, Validation. **Dan Li:** Methodology. **Yujie Chen:** Software. **Chunhua Wang:** Formal analysis. **Guige Hou:** Formal analysis. **Thorsten Steinberg:** Resources. **Bernd Rolauffs:** Resources. **Mohamed EL-Newehy:** Resources. **Hany EL-Hamshary:** Resources. **Jia Jiang:** Funding acquisition, Investigation. **Xiumei Mo:** Supervision, Project administration, Funding acquisition. **Jinzhong Zhao:** Supervision, Funding acquisition.

Jinglei Wu: Supervision, Project administration.

Declaration of competing interest

The authors declare that they have no known competing financial interests or personal relationships that could have appeared to influence the work reported in this paper.

Appendix A. Supplementary data

Supplementary data to this article can be found online at https://doi.org/10.1016/j.bioactmat.2023.08.004.

References

[1] K.E. Webster, Return to sport and reinjury rates in elite female athletes after anterior cruciate ligament rupture, Sports Med. 51 (4) (2021) 653–660.
[2] Y. Tang, J. Tian, L. Li, L. Huang, Q. Shen, S. Guo, Y. Jiang, Biomimetic biphasic electrospun scaffold for anterior cruciate ligament tissue engineering, Tissue Eng. Regener. Med. 18 (5) (2021) 819–830.
[3] J. Cai, Q. Zhang, J. Chen, J. Jiang, X. Mo, C. He, J. Zhao, Electrodeposition of calcium phosphate onto polyethylene terephthalate artificial ligament enhances graft-bone integration after anterior cruciate ligament reconstruction, Bioact. Mater. 6 (3) (2021) 783–793.
[4] O. Evrova, G.M. Burgisser, C. Ebnother, A. Adathala, M. Calcagni, E. Bachmann, J. G. Snedeker, C. Scalera, P. Giovanoli, V. Vogel, J. Buschmann, Elastic and surgeon friendly electrospun tubes delivering PDGF-BB positively impact tendon rupture healing in a rabbit Achilles tendon model, Biomaterials 232 (2020), 119722.
[5] T. Lei, T. Zhang, W. Ju, X. Chen, B.C. Heng, W. Shen, Z. Yin, Biomimetic strategies for tendon/ligament-to-bone interface regeneration, Bioact. Mater. 6 (8) (2021) 2491–2510.
[6] M. Beldjilali-Labro, A. Garcia Garcia, F. Farhat, F. Bedoui, J.F. Grosset, M. Dufresne, C. Legallais, Biomaterials in tendon and skeletal muscle tissue engineering: current trends and challenges, Materials 11 (7) (2018) 1116–1164.
[7] T. Chen, P. Zhang, J. Chen, Y. Hua, S. Chen, Long-term outcomes of anterior cruciate ligament reconstruction using either synthetics with remnant preservation or hamstring autografts: a 10-year longitudinal study, Am. J. Sports Med. 45 (12) (2017) 2739–2750.
[8] T.M. Tiefenboeck, E. Thurmaier, M.M. Tiefenboeck, R.C. Ostermann, J. Joestl, M. Winnisch, M. Schurz, S. Hajdu, M. Hofbauer, Clinical and functional outcome after anterior cruciate ligament reconstruction using the LARS™ system at a minimum follow-up of 10years, Knee 22 (6) (2015) 565–568.
[9] H. Lui, R. Bindra, J. Baldwin, S. Ivanovski, C. Vaquette, Additively manufactured multiphasic bone-ligament-bone scaffold for scapholunate interosseous ligament reconstruction, Adv. Healthcare Mater. 8 (14) (2019), e1900133.
[10] S.K. Madhurakkat Perikamana, J. Lee, T. Ahmad, E.M. Kim, H. Byun, S. Lee, H. Shin, Harnessing biochemical and structural cues for tenogenic differentiation of adipose derived stem cells (ADSCs) and development of an in vitro tissue interface mimicking tendon-bone insertion graft, Biomaterials 165 (2018) 79–93.
[11] P. Zhang, F. Han, T. Chen, Z. Wu, S. Chen, "Swiss roll"-like bioactive hybrid scaffolds for promoting bone tissue ingrowth and tendon-bone healing after anterior cruciate ligament reconstruction, Biomater. Sci. 8 (3) (2020) 871–883.

[12] Q. Dong, J. Cai, H. Wang, S. Chen, Y. Liu, J. Yao, Z. Shao, X. Chen, Artificial ligament made from silk protein/Laponite hybrid fibers, Acta Biomater. 106 (2020) 102–113.

[13] S. Wu, Y. Wang, P.N. Streubel, B. Duan, Living nanofiber yarn-based woven biotextiles for tendon tissue engineering using cell tri-culture and mechanical stimulation, Acta Biomater. 62 (2017) 102–115.

[14] J. Wang, H. Xiong, T. Zhu, Y. Liu, H. Pan, C. Fan, X. Zhao, W.W. Lu, Bioinspired multichannel nerve guidance conduit based on shape memory nanofibers for potential application in peripheral nerve repair, ACS Nano 14 (10) (2020) 12579–12595.

[15] J. Cai, J. Liu, J. Xu, Y. Li, T. Zheng, T. Zhang, K. Han, S. Chen, J. Jiang, S. Wu, J. Zhao, Constructing high-strength nano-micro fibrous woven scaffolds with native-like anisotropic structure and immunoregulatory function for tendon repair and regeneration, Biofabrication 15 (2) (2023) 025002.

[16] I. Calejo, R. Costa-Almeida, R.L. Reis, M.E. Gomes, A textile platform using continuous aligned and textured composite microfibers to engineer tendon-to-bone interface gradient scaffolds, Adv. Healthcare Mater. 8 (15) (2019), 1900200.

[17] C. Gogele, J. Vogt, J. Hahn, A. Breier, R. Bernhardt, M. Meyer, M. Schropfer, K. Schafer-Eckart, G. Schulze-Tanzil, Co-culture of mesenchymal stem cells and ligamentocytes on triphasic embroidered poly(L-lactide-co-epsilon-caprolactone) and polylactic acid scaffolds for anterior cruciate ligament enthesis tissue engineering, Int. J. Mol. Sci. 24 (7) (2023) 6714–6733.

[18] M. Kokozidou, C. Gogele, F. Pirrung, N. Hammer, C. Werner, B. Kohl, J. Hahn, A. Breier, M. Schropfer, M. Meyer, G. Schulze-Tanzil, In vivo ligamentogenesis in embroidered poly(lactic-co-epsilon-caprolactone)/polylactic acid scaffolds functionalized by fluorination and hexamethylene diisocyanate cross-linked collagen foams, Histochem. Cell Biol. 159 (3) (2023) 275–292.

[19] A. Teuschl, P. Heimel, S. Nürnberger, M. van Griensven, H. Redl, T. Nau, A novel silk fiber-based scaffold for regeneration of the anterior cruciate ligament: histological results from a study in sheep, Am. J. Sports Med. 44 (6) (2016) 1547–1557.

[20] M.N. Collins, G. Ren, K. Young, S. Pina, R.L. Reis, J.M. Oliveira, Scaffold fabrication technologies and structure/function properties in bone tissue engineering, Adv. Funct. Mater. 31 (21) (2021) 2010609.

[21] X. Xie, J. Cai, Y. Yao, Y. Chen, A.u.R. Khan, J. Wu, X. Mo, A woven scaffold with continuous mineral gradients for tendon-to-bone tissue engineering, Composites, Part B 212 (2021), 108679.

[22] F. Xie, Y. Wang, L. Zhuo, F. Jia, D. Ning, Z. Lu, Electrospun wrinkled porous polyimide nanofiber-based filter via thermally induced phase separation for efficient high-temperature PMs capture, ACS Appl. Mater. Interfaces 12 (50) (2020) 56499–56508.

[23] G. Conoscenti, T. Schneider, K. Stoelzel, F. Carfi Pavia, V. Brucato, C. Goegele, V. La Carrubba, G. Schulze-Tanzil, PLLA scaffolds produced by thermally induced phase separation (TIPS) allow human chondrocyte growth and extracellular matrix formation dependent on pore size, Mater. Sci. Eng. C 80 (2017) 449–459.

[24] G. Conoscenti, F. Carfi Pavia, A. Ongaro, V. Brucato, C. Goegele, S. Schwarz, A. R. Boccaccini, K. Stoelzel, V. La Carrubba, G. Schulze-Tanzil, Human nasoseptal chondrocytes maintain their differentiated phenotype on PLLA scaffolds produced by thermally induced phase separation and supplemented with bioactive glass 1393, Connect, Tissue Res 60 (4) (2019) 344–357.

[25] Z. Li, H. Liu, R. Wang, C. Ji, Y. Wei, M. Shi, Y. Wang, Y. Du, Y. Zhang, Q. Yuan, C. Yan, Bioactive core-shell CaF2 upconversion nanostructure for promotion and visualization of engineered bone reconstruction, ACS Nano 14 (11) (2020) 16085–16095.

[26] Y. Yan, H. Chen, H. Zhang, C. Guo, K. Yang, K. Chen, R. Cheng, N. Qian, N. Sandler, Y.S. Zhang, H. Chen, J. Qi, W. Cui, L. Deng, Vascularized 3D printed scaffolds for promoting bone regeneration, Biomaterials 190–191 (2019) 97–110.

[27] Y. Li, W. Tjandra, K.C. Tam, Synthesis and characterization of nanoporous hydroxyapatite using cationic surfactants as templates, Mater. Res. Bull. 43 (8) (2008) 2318–2326.

[28] Y. Wang, W. Cui, X. Zhao, S. Wen, Y. Sun, J. Han, H. Zhang, Bone remodeling-inspired dual delivery electrospun nanofibers for promoting bone regeneration, Nanoscale 11 (1) (2018) 60–71.

[29] X. Liu, X. He, D. Jin, S. Wu, H. Wang, M. Yin, A. Aldalbahi, M. El-Newehy, X. Mo, J. Wu, A biodegradable multifunctional nanofibrous membrane for periodontal tissue regeneration, Acta Biomater. 108 (2020) 207–222.

[30] K. Zhang, Y. Zhou, C. Xiao, W. Zhao, X. Zhang, Application of hydroxyapatite nanoparticles in tumor-associated bone segmental defect, Sci. Adv. 5 (8) (2019) 6946–6962.

[31] V. Musahl, A. Lehner, Y. Watanabe, F.H. Fu, Biology and biomechanics, Curr. Opin. Rheumatol. 14 (2) (2002) 127–133.

[32] F. Wu, J. Zheng, Z. Li, M. Liu, Halloysite nanotubes coated 3D printed PLA pattern for guiding human mesenchymal stem cells (hMSCs) orientation, Chem. Eng. J. 359 (2019) 672–683.

[33] W. Liu, J. Lipner, J. Xie, C.N. Manning, S. Thomopoulos, Y. Xia, Nanofiber scaffolds with gradients in mineral content for spatial control of osteogenesis, ACS Appl. Mater. Interfaces 6 (4) (2014) 2842–2849.

[34] J. Cai, J. Xu, Z. Ye, L. Wang, T. Zheng, T. Zhang, Y. Li, J. Jiang, J. Zhao, Exosomes derived from Kartogenin-preconditioned mesenchymal stem cells promote cartilage formation and collagen maturation for enthesis regeneration in a rat model of chronic rotator cuff tear, Am. J. Sports Med. 51 (5) (2023) 1267–1276.

[35] Z. Yuan, Z. Wan, C. Gao, Y. Wang, J. Huang, Q. Cai, Controlled magnesium ion delivery system for in situ bone tissue engineering, J. Contr. Release 350 (2022) 360–376.

[36] M.P. Prabhakaran, J. Venugopal, S. Ramakrishna, Electrospun nanostructured scaffolds for bone tissue engineering, Acta Biomater. 5 (8) (2009) 2884–2893.

[37] S. Suvarnapathaki, X. Wu, D. Lantigua, M.A. Nguyen, G. Camci-Unal, Hydroxyapatite-incorporated composite gels improve mechanical properties and bioactivity of bone scaffolds, Macromol. Biosci. 20 (10) (2020), e2000176.

[38] A. De Luca, I. Vitrano, V. Costa, L. Raimondi, V. Carina, D. Bellavia, G. Conoscenti, R. Di Falco, F.C. Pavia, V. La Carrubba, V. Brucato, G. Giavaresi, Improvement of osteogenic differentiation of human mesenchymal stem cells on composite poly l-lactic acid/nano-hydroxyapatite scaffolds for bone defect repair, J. Biosci. Bioeng. 129 (2) (2020) 250–257.

[39] A. Donneys, D.M. Weiss, S.S. Deshpande, S. Ahsan, C.N. Tchanque-Fossuo, D. Sarhaddi, B. Levi, S.A. Goldstein, S.R. Buchman, Localized deferoxamine injection augments vascularity and improves bony union in pathologic fracture healing after radiotherapy, Bone 52 (1) (2013) 318–325.

[40] J. Drager, J.L. Ramirez-GarciaLuna, A. Kumar, U. Gbureck, E.J. Harvey, J. E. Barralet, Hypoxia biomimicry to enhance monetite bone defect repair, Tissue Eng., Part A 23 (23–24) (2017) 1372–1381.

[41] Q. Jiang, L. Wang, Z. Liu, J. Su, Y. Tang, P. Tan, X. Zhu, K. Zhang, X. Ma, J. Jiang, J. Zhao, H. Lin, X. Zhang, Canine ACL reconstruction with an injectable hydroxyapatite/collagen paste for accelerated healing of tendon-bone interface, Bioact. Mater. 20 (2023) 1–15.

[42] P. Weimin, L. Dan, W. Yiyong, Z. Hunyu, Z. Li, Tendon-to-bone healing using an injectable calcium phosphate cement combined with bone xenograft/BMP composite, Biomaterials 34 (38) (2013) 9926–9936.

[43] Y. Zha, T. Lin, Y. Li, X. Zhang, Z. Wang, Z. Li, Y. Ye, B. Wang, S. Zhang, J. Wang, Exosome-mimetics as an engineered gene-activated matrix induces in-situ vascularized osteogenesis, Biomaterials 247 (2020), 119985.

[44] X. Han, M. Sun, B. Chen, Q. Saiding, J. Zhang, H. Song, L. Deng, P. Wang, W. Gong, W. Cui, Lotus seedpod-inspired internal vascularized 3D printed scaffold for bone tissue repair, Bioact. Mater. 6 (6) (2021) 1639–1652.

[45] P. Jia, H. Chen, H. Kang, J. Qi, P. Zhao, M. Jiang, L. Guo, Q. Zhou, N.D. Qian, H. B. Zhou, Y.J. Xu, Y. Fan, L.F. Deng, Deferoxamine released from poly(lactic-co-glycolic acid) promotes healing of osteoporotic bone defect via enhanced angiogenesis and osteogenesis, J. Biomed. Mater. Res., Part A 104 (10) (2016) 2515–2527.

[46] Q. Ran, Y. Yu, W. Chen, X. Shen, C. Mu, Z. Yuan, B. Tao, Y. Hu, W. Yang, K. Cai, Deferoxamine loaded titania nanotubes substrates regulate osteogenic and angiogenic differentiation of MSCs via activation of HIF-1α signaling, Mater. Sci. Eng. C 91 (2018) 44–54.

[47] A.P. Kusumbe, S.K. Ramasamy, R.H. Adams, Coupling of angiogenesis and osteogenesis by a specific vessel subtype in bone, Nature 507 (7492) (2014) 323–328.

[48] X. Li, S. Pongkitwitoon, H. Lu, C. Lee, R. Gelberman, S. Thomopoulos, CTGF induces tenogenic differentiation and proliferation of adipose-derived stromal cells, J. Orthop. Res. 37 (3) (2019) 574–582.

[49] X.X. Cong, X.S. Rao, J.X. Lin, X.C. Liu, G.A. Zhang, X.K. Gao, M.Y. He, W.L. Shen, W. Fan, D. Pioletti, L.L. Zheng, H.H. Liu, Z. Yin, B.C. Low, R. Schweitzer, H. Ouyang, X. Chen, Y.T. Zhou, Activation of AKT-mTOR signaling directs tenogenesis of mesenchymal stem cells, Stem Cell. 36 (4) (2018) 527–539.

[50] H. Shen, R. Jayaram, S. Yoneda, S.W. Linderman, S.E. Sakiyama-Elbert, Y. Xia, R. H. Gelberman, S. Thomopoulos, The effect of adipose-derived stem cell sheets and CTGF on early flexor tendon healing in a canine model, Sci. Rep. 8 (1) (2018), 11078.

[51] N. Pramanik, T. Imae, Fabrication and characterization of dendrimer-functionalized mesoporous hydroxyapatite, Langmuir 28 (39) (2012) 14018–14027.

[52] J. Chu, L. Chen, Z. Mo, G.L. Bowlin, B.A. Minden-Birkenmaier, Y. Morsi, A. Aldalbahi, M. El-Newehy, W. Wang, X. Mo, An atorvastatin calcium and poly(L-lactide-co-caprolactone) core-shell nanofiber-covered stent to treat aneurysms and promote reendothelialization, Acta Biomater. 111 (2020) 102–117.

[53] J. Cai, X. Xie, D. Li, L. Wang, J. Jiang, X. Mo, J. Zhao, A novel knitted scaffold made of microfiber/nanofiber core-sheath yarns for tendon tissue engineering, Biomater. Sci. 8 (16) (2020) 4413–4425.

[54] X. Xie, J. Xu, J. Lin, J. Jiang, Y. Huang, J. Lu, Y. Kang, Y. Hu, J. Cai, F. Wang, T. Zhu, J. Zhao, L. Wang, A regeneration process-matching scaffold with appropriate dynamic mechanical properties and spatial adaptability for ligament reconstruction, Bioact. Mater. 13 (2022) 82–95.